Low melting temperature gallium-indium liquid metal anode for solid-state Li-ion batteries

Hua Wang[1,2], Xintong Li[1], Tianyi Li[3], Xi Chelsea Chen[4], Kai Chang[1], Lei Chen[5], Zhenzhen Yang[6] and Likun Zhu[1,2*]

[1]Department of Mechanical and Energy Engineering, Indiana University Purdue University Indianapolis, Indianapolis, IN 46202, USA
[2]School of Mechanical Engineering, Purdue University, West Lafayette, IN 47907, USA
[3]Advanced Photon Source, Argonne National Laboratory, Lemont, IL 60439, USA
[4]Chemical Sciences Division, Oak Ridge National Laboratory, Oak Ridge, TN 37830, USA
[5]Department of Mechanical Engineering, University of Michigan-Dearborn, Dearborn, MI 48128, USA
[6]Chemical Science and Engineering Division, Argonne National Laboratory, Lemont, IL 60439, USA

[*]Corresponding author: Likun Zhu, zhu154@purdue.edu

Abstract

Solid-state Li-ion batteries are attracting attention for their enhanced safety features, higher energy density, and broader operational temperature range compared to systems based on liquid electrolytes. However, current solid-state Li-ion batteries face performance challenges, such as suboptimal cycling and poor rate capabilities, often due to inadequate interfacial contact between the solid electrolyte and electrodes. To address this issue, we incorporated a gallium-indium (Ga-In) liquid metal as the anode in a solid-state Li-ion battery setup, employing Li_6PS_5Cl as the solid electrolyte. Operating at room temperature, this configuration achieved an initial capacity of 389 mAh g^{-1} and maintained 88% of this capacity after 30 cycles at a 0.05 C rate. It also demonstrated a capacity retention of 66% after 500 cycles at a 0.5 C rate. In comparison to solid anode materials, such as tin, the Ga-In liquid metal exhibited superior cycling stability and rate capacity, which is due to the self-healing and fluid properties of the alloy that ensure stable interfacial contact with solid electrolytes. In-situ XRD and ex-situ SEM analyses revealed that indium does not directly participate in the lithiation/delithiation process. Instead, it helps maintain the alloy's low melting point, facilitating its return to a liquid state after delithiation. In a comparative analysis of stack pressure during cycling in cells utilizing Ga-In liquid metal and tin, the Ga-In liquid metal cell demonstrated an ability to buffer pressure increases associated with deformation. These findings suggest a promising approach for enhancing solid-state batteries by integrating liquid metal anodes, which improve interfacial contact and stability.

Keywords: Gallium-indium, liquid metal, solid-state batteries, interfacial contact, stack pressure

Introduction

Energy storage has become a critical field of research, with Li-ion batteries (LIBs) emerging as the predominant power sources. They are particularly promising for portable electronic devices, electric vehicles (EVs), and large-scale energy storage systems, owing to their exceptional energy density [1]. However, as more EVs take to the roads and high-energy-density LIBs are increasingly used in energy storage systems, the volatile and flammable liquid electrolyte in current commercial LIBs raises significant safety concerns. Auxiliary safety monitoring subsystems are usually required in battery packs to mitigate fire hazards, which in turn reduces the energy density of the pack. Solid-state LIBs, which utilize highly conductive and nonflammable solid electrolytes, are being viewed as a promising alternative to overcome the safety and energy density challenges associated with traditional liquid electrolyte-based LIBs. Due to its high ionic conductivity, sulfide solid electrolytes are considered the most promising materials for solid-state batteries (SSBs). Among various sulfide electrolytes, Li_6PS_5X (X=Cl, Br, I) stands out for its wide electrochemical window and cost-effective precursors, making it a strong candidate for future solid electrolyte applications. Although, Li_6PS_5Cl was reported as the most stable among these compounds (Li_6PS_5Cl, Li_6PS_5Br and Li_6PS_5I), all of them can be decomposed in contact with lithium metal [2, 3]. Substitution with Li-M alloy (M = In, Si, Sn and Al etc.) is one strategy to avoid interfacial reactions, but it results in a lower working voltage and reduced capacity [4]. Despite the high ionic conductivity of solid electrolytes, solid-state LIBs struggle to match the specific capacity, rate capability, and cycle life of their liquid electrolyte counterparts. This performance gap is mainly attributed to the solid electrolytes' poor interfacial contact with solid electrodes, primarily because of the volume changes in electrode materials during charging and discharging. For instance, high-capacity Li-alloy materials like silicon (Si), germanium (Ge), and tin (Sn) experience substantial volume changes during lithiation and delithiation reactions, which can lead to mechanical fractures in the anode particles. This may disrupt connections within electronically and ironically conductive networks [5-15]. Such damage ultimately leads to the deactivation of the active materials and results in a reduced cycle life of the electrodes. To solve the interface issue in SSBs, applying uniaxial stress, known as "stack pressure", is a widely adopted method to initiate and sustain the contact between active materials and the solid electrolyte. Numerous studies have employed high stack pressures, with some exceeding 200 MPa [16-23]. However, achieving such high stack pressures is

challenging and costly in practical applications, posing a significant barrier to the commercial viability of these batteries [24].

In contrast, the liquid-solid interface in traditional LIBs allows the liquid electrolyte to fully infiltrate the electrodes, enhancing Li-ion transport across the entire surface of the active material particles. Exploiting the advantages of the liquid-solid interface in SSBs could significantly enhance their performance. One viable strategy to achieve this is by replacing solid electrode materials with liquid ones [25]. This substitution could potentially improve the interfacial contact, ensuring better ionic conduction and facilitating charge and discharge processes. Liquid electrodes can inherently accommodate the volumetric changes that occur during the battery's charge and discharge cycles, mitigating mechanical stresses and potentially prolonging the battery's lifespan. Furthermore, the inherent fluidity of liquid electrode materials can lead to better contact with the solid electrolyte, ensuring a more effective ion transport.

Recently, there has been growing interest in exploring low-melting-point liquid metals as anode materials in liquid electrolyte, particularly due to their self-healing properties. Gallium (Ga) is notable in this context, distinguished by its exceptionally low melting point of 29.8 ℃ and its theoretical capacity of 769 mAh g^{-1}. This makes it an attractive option for liquid-metal anodes. Research by Deshpande et al., along with other studies in 2011, identified Ga as a promising material for this application [26, 27]. Wu et al. achieved notable cycling performance with a Ga-Sn alloy integrated into a structure of reduced graphene oxide and carbon nanotubes, showcasing self-healing characteristics [15]. Additionally, Guo et al. utilized a Ga-In alloy, with a very low melting point of 15 ℃, in Li-ion and Na-ion batteries, exhibiting promising cyclic durability and capacity [28]. However, liquid metal alternates between liquid and solid states during discharge and charge cycles, leading to the formation of a solid electrolyte interphase (SEI) and the progressive depletion of Li within the battery. To mitigate these issues, solid electrolytes can be employed to enhance the stability of the interface. Additionally, the fluidity of the liquid metal aids in sustaining consistent contact with the solid electrolyte. To this end, limited research has been conducted on the application of liquid metal in SSBs. Luo et al. developed a low-melting alloy interlayer using a simple in situ reaction for solid-state lithium metal batteries. The results show that the battery with the Ga–In–Sn–Li alloy interlayer demonstrates excellent cycling and rate performance due to

the alloy's superior chemical stability and mechanical properties [29]. Li et al. presented a SSB design with a PEO-based solid electrolyte and a Ga-Sn alloy anode at 60 ℃, which exhibited improved cycling performance due to the fluidity of liquid metal [30]. Mo et al. developed a SSB using a GaSb anode and a $LiBH_4$ solid electrolyte at 125 ℃, where they observed the in situ generation of liquid metal Ga. The presence of liquid Ga at the Sb/$LiBH_4$ interface improves wetting, alleviates internal stress, and accelerates the diffusion of both electrons and ions, thereby enhancing the electrochemical performance of the Sb metal. [25] However, the operation of these SSBs at elevated temperatures is required due to the low Li-ion conductivity of PEO and $LiBH_4$ at room temperature. This requirement for high-temperature operation not only restricts the range of potential applications but also diminishes the energy density of the battery system. The need for thermal management systems to maintain optimal operating temperatures complicates the battery design, and increases the weight and cost of the battery system.

In this study, we aim to explore the feasibility of a solid-state LIB that operates efficiently at room temperature, utilizing the lower melting point of Ga-In alloys and the high Li-ion conductivity of sulfide-based solid electrolytes. This approach is intended to enhance the battery's cycling stability by taking advantage of the fluidity and self-healing properties of Ga-In alloys. First, we investigated the performance of Ga-In liquid metal as anode material in SSBs, using Li_6PS_5Cl as solid electrolyte and Lithium-Aluminum (Li-Al) alloy as Li resource. The reaction mechanism of Ga-In alloy as anode was investigated by in-situ X-ray Diffraction (XRD). The effect of stack pressure on battery performance was evaluated on both Ga-In liquid metal anode and solid Sn anode. Additionally, we monitored stack pressure evolution during discharge and charge in SSB full cells using $LiNi_{0.33}Mn_{0.33}Co_{0.33}O_2$ (NMC111). Finally, the cycling stability, rate capability and AC impedance of the solid battery were presented and discussed.

Experimental

Materials

Gallium-Indium alloy (Ga-In, 75.5:24.5 wt%, Sigma-Aldrich), Tin powder (Sn, 300 nm, 99.9% trace metals basis, US Research Nanomaterials Inc.), NMC111 ($LiNi_{0.33}Mn_{0.33}Co_{0.33}O_2$, Umicore), Sulfide solid electrolyte (Li_6PS_5Cl, 1 μm, 99.9%, Ampcera Inc.) Super C65 (conductive carbon black, Timcal Co., Ltd.), polyvinylidene fluoride (PVDF, 12wt%, Kureha Battery Materials Japan

Co., Ltd.), 1-methyl-2-pyrrolidinone (NMP, anhydrous 99.5%, Sigma-Aldrich), 1M LiPF6 in ethylene carbonate and dimethyl carbonate solution mixed as 1:1 vol ratio (BASF Corporation), Li ribbon (thickness 0.38mm, 99.9% trace metals basis, Sigma-Aldrich), Li-Al alloy powder (Li-Al, 50:50 wt%, Sigma-Aldrich) were purchased and used as received.

Preparation of liquid metal alloy (Ga-In)

The liquid metal alloy was added into a small vial, to which sodium dodecyl sulfate (SDS) and acetonitrile were added as the surfactant and solvent, respectively, at a ratio of 1 mg of SDS to 50 mg of liquid metal alloy. The purpose of using SDS was to facilitate the reduction in size of the liquid metal particles during sonication, as documented in the literature [28]. Subsequently, the mixture containing large liquid metal droplets underwent probe ultrasonication using a Sonics Vibracell VC505 sonicator for 5 min, with an operational cycle of 2 seconds on followed by 2 seconds off. This process was aimed at breaking down the large liquid metal droplets into finer particles. Afterward, the suspension underwent further ultrasonication in a beaker for 30 min, with cold water employed to maintain a cool temperature. Post-ultrasonication, the suspension was dried to obtain a powder, which was then used in the fabrication of the electrode.

Fabrication of electrode

For solid-state LIB experiments, Ga-In and Sn electrodes were fabricated from a mixture of active material (either Ga-In powder or nano-Sn powder) and binder (PVDF), with a mass ratio of 95:5. This mixture was combined with NMP solvent, then stirred continuously for 24 h using a magnetic stir bar to ensure homogeneity. The uniformly mixed slurry was then cast onto a copper foil using a doctor blade technique and subsequently dried under vacuum at 100℃ for 24 h. The resulting dried electrodes were then punched into discs of approximately 0.5 cm^2 (with a diameter of 8 mm) and a mass loading of 0.6 mg cm^{-2}. These discs were then transferred to an argon-filled glovebox for subsequent processing and testing. For the in-situ XRD experiment, Ga-In electrode was fabricated from a mixture of Ga-In powder, super C65 and binder (PVDF), with a mass ratio of 5:3:2 following same process as above.

Battery assembly

Coin cell

The fabrication of cells, specifically CR2032 coin cells, was carried out in an argon-filled glovebox. The process commenced with the positioning of a stainless-steel disc inside the coin cell casing. Next, an electrode was placed on the disc with the copper side facing downwards. Subsequently, 30 µL of electrolyte was delicately dispensed onto the electrode. This was followed by the placement of a Celgard 2400 separator on the wetted electrode. Another 30 µL electrolyte was then added on top of the separator to ensure proper saturation. Following this, a piece of Li metal was positioned over the separator, and a stainless-steel disc was used to encase the Li metal. To complete the assembly, a spring was inserted beneath the opposite side of the coin cell case to act as a spacer. The cell was then securely crimped to ensure integrity and was removed from the glovebox in preparation for subsequent electrochemical evaluation.

In-situ coin cell

To facilitate X-ray penetration through the CR2032 coin cell casing, the coin cells were modified for in-situ experiments. Holes with a diameter of 2 mm were precision-punched at the center of both the anode and cathode cases. These holes were then sealed with 30 µm-thick Kapton tape, applied to both sides of each case. The stainless-steel discs were similarly punched to create corresponding holes. The assembly process was the same as assembly of coin cell. Once assembled, the cell underwent a crimping process and was then removed from the glovebox for in-situ XRD experiments.

Solid-state battery half cell (SSB-H)

The fabrication of SSB-Hs took place within an argon-filled glovebox. Initially, Li-Al alloy powder (20 mg) was positioned in a pressing die sleeve (9 mm in diameter) and compressed under approximately 400 MPa for 10 min. Following this, solid electrolyte powder was layered over the compressed Li-Al film and subjected to the same pressing process, again at approximately 400 MPa for 10 min. An electrode, with its copper side facing up, was then placed on the electrolyte film. Afterward, a plunger rod equipped with an O-ring was used to seal the assembly, and the stack pressure was adjusted accordingly.

Solid-state battery full cell (SSB-F) for stack pressure monitoring experiment

The fabrication of SSB-Fs for pressure monitoring was conducted using the SSB-H assembly procedures described above, with modifications made to the cathode and anode films. The cathode films were compressed under 400 MPa for 10 min using a mixture of NMC111, Super C65, and Li_6PS_5Cl in a mass ratio of 6:1:3. The anode films were similarly compressed under 400 MPa for 10 min using a mixture of Ga-In powder (or nano-Sn powder) with Li_6PS_5Cl in a mass ratio of 7:3. The capacity ratio of anode and cathode was set as 1:1.2 to maximize the involvement of anode material in lithiation and delithiation reactions. A pressure sensor was placed in the SSB-F assembly to monitor the pressure variation. An initial stack pressure of 20 MPa was applied to the Sn SSB-F, and a slightly lower pressure of 15 MPa was applied to the Ga-In SSB-F to prevent short-circuiting due to the fluid nature of Ga-In. After assembly, the stack pressure began to decrease as the material particles reorganized. The battery cells were left to rest for approximately 24 h to allow the stack pressure to stabilize, before starting the cycling process.

Table 1 presents the configurations and corresponding experiments for the four types of battery cells.

Table 1. Battery cell names in manuscript with their configurations and performed experiments.

Battery Cell Name	**Battery Configuration**	**Performed Experiments**
Coin cell	Electrode// separator//Li metal with liquid electrolyte	CV
In-situ coin cell	Electrode// separator//Li metal with liquid electrolyte, and holes on cases	In-situ synchrotron XRD
SSB-H	Electrode// solid electrolyte//Li-Al	CV, EIS, cycling, and rate capability
SSB-F	Electrode// solid electrolyte//NMC	Stack pressure monitoring

Electrochemical evaluation

The cells were connected to an Arbin BT2000 battery cycler for evaluation at room temperature. Prior to the cycling process, the cells were initially rested for 30 min. According to the mass of active material in the cell, the cells were cycled galvanostatically at C/20 and C/2 rate (1C = 835 mA g^{-1} for Ga-In weight), in a voltage range between 0.01 V and 2.0 V. Cyclic voltammetry (CV) analyses were performed at room temperature using a BioLogic VSP workstation, in which the potential was set to sweep from open-circuit voltage to 0.01 V and then to sweep back to 3.0 V (with Li metal) or 2.0 V (with Li-Al) at a 0.1 mV s^{-1} scanning rate. Electrochemical impedance spectroscopy (EIS) was also conducted by the VSP workstation in the frequency range from 5×10^5 to 0.1 Hz with an amplitude of 5 mV.

Scanning electron microscopy

The electrodes underwent morphological characterization using a JEOL JSM-7800F Field Emission Scanning Electron Microscope (FE-SEM).

In-situ synchrotron XRD

The synchrotron XRD experiment was conducted at the Advanced Photon Source (APS) on beamline 17-BM. The photon source had a wavelength of 0.24114 Å and an energy of 51 keV. The size of the incident beam, which was utilized on the sample, was precisely 500 μm by 500 μm. The experiment was conducted using the transmission mode, where the detector was strategically positioned at a distance of 700 mm from the sample. The scattering intensity was captured using a 2D Varex area detector, with each pixel size of 150 μm and the total array consisting of 2880 by 2880 pixels. The 2D diffraction patterns produced by the synchrotron XRD were calibrated employing a standard cerium dioxide sample. The in-situ cell was cycling at 0.2 C with a current density of 0.08 mA for mass loading 0.6 mg cm^{-2}. Furthermore, the 2D patterns were converted to 1D patterns through the application of GSAS II software.

X-ray photoelectron spectroscopy (XPS) analysis

The XPS measurements were performed utilizing a PHI 5000 VersaProbe II system with a monochromatized Al Kα radiation (hν = 1486.6 eV) beam at the Argonne National Lab. A pass energy of 23.5 eV was utilized to collect the high-resolution spectrum. The analysis chamber

maintained a pressure of approximately 10^{-8} Torr. Samples were transferred to the chamber without air exposure.

Results and discussion

Fig. 1a illustrates the SEM images of the pristine Ga-In electrode, showcasing that the Ga-In alloy was effectively ultrasonicated into uniformly sized nanoscale particles. However, after undergoing cycling in SSB-H under 20 MPa, the Ga-In alloy adhered to the solid electrolyte surface forms droplets of various sizes, as depicted in Fig. 1b, with some expanding to the micron scale. These Ga-In droplets are believed to participate actively in the lithiation and delithiation processes, given their attachment to the solid electrolyte, suggesting that the Ga-In alloy manages to regain its structure post-delithiation. The transformation into larger, micron-sized droplets is likely influenced by the lithiation process or the high stacking pressure. The spherical shape of Ga-In droplets on the solid electrolyte indicates that the Ga-In liquid alloy does not exhibit significant spreading on the solid electrolyte surface. As shown in Fig. S1, the contact angle of the Ga-In liquid metal on a Li_6PS_5Cl solid electrolyte was measured to be 134.9˚. A contact angle smaller than 90˚ would signify improved wettability. However, enhanced wettability also increases the risk of liquid metal penetrating the solid electrolyte separator, potentially leading to a short circuit in the battery. Even with the high contact angle, there is a possibility of Ga-In liquid metal alloy penetrating the electrolyte in this battery system at high pressure, because of the fluidity of Ga-In liquid metal. To mitigate this, it is essential to operate under relatively low pressure to prevent penetration. Alternatively, a seamless electrolyte layer can be applied to prevent penetration. Further analysis is provided in Fig. 1c, which presents the EDX imaging of Ga-In droplets on the solid electrolyte surface, extracted from a cycled Ga-In SSB-H. Here, the elemental distribution demonstrates that indium is consistently present with gallium across the droplets. This continuity implies that indium remains alloyed with gallium after the cycling process, contributing to a liquid alloy that retains a low melting point. Consequently, this alloy remains in a liquid state at room temperature, which is critical for the battery's operational stability and performance. This finding underscores the robustness of the Ga-In alloy in maintaining its compositional integrity and liquid state throughout the battery's charge-discharge cycles, which is pivotal for ensuring consistent electrochemical performance and enhancing the battery's cycling stability.

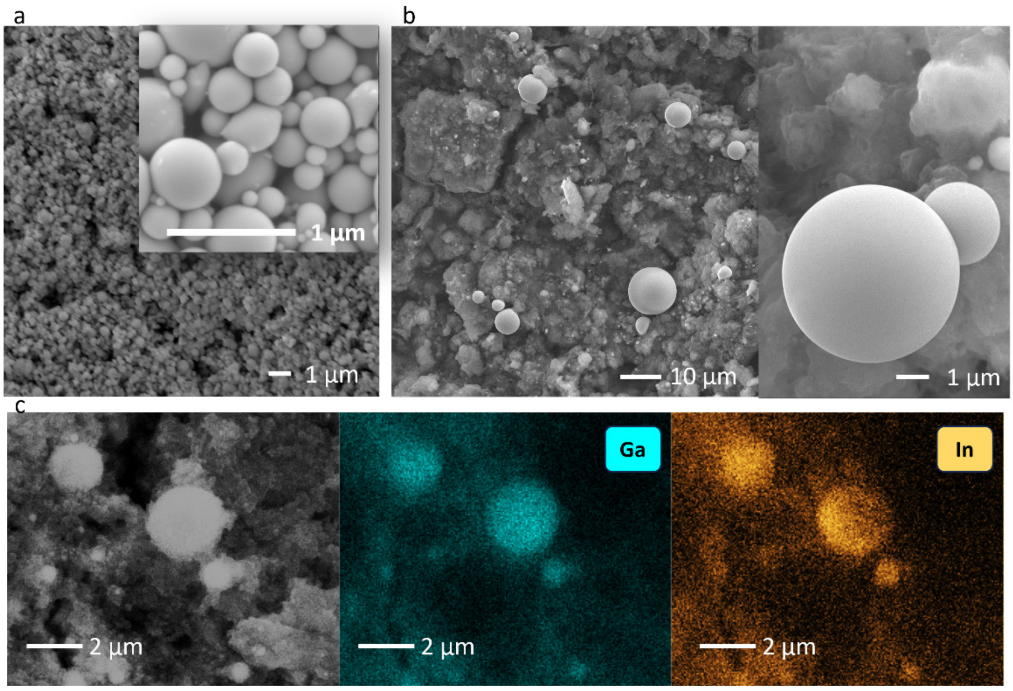

Figure 1. a) SEM image of a Ga-In electrode, where the upper right corner is ultrasonicated nanosized Ga-In droplets; b) SEM image Ga-In droplets on the solid electrolyte surface from a disassembled cycled Ga-In SSB-H under 20 MPa; c) EDX image of Ga-In droplets on the solid electrolyte surface, taken from a disassembled cycled Ga-In SSB-H under 20 MPa.

To investigate the lithiation/delithiation mechanisms of the Ga-In alloy, we performed in-situ XRD analysis to examine the reactions occurring within the Ga-In electrode during the discharge and charge processes. Fig. 2 shows the contour map of in-situ XRD patterns for a pristine cell within an EC/DEC electrolyte and the voltage profile, cycled at a rate of 0.2 C. Initially, the XRD pattern plots (Fig. S2) reveals peaks at 4.11˚, 6.47˚, and 6.79˚, attributed to carbon, and a peak at 5.58˚, ascribed to Li, with no discernible peaks for Ga-In, indicating its amorphous and liquid state on the electrode. As shown in Fig. 2a, a new peak at 5.07˚ emerges at 0.65V during discharge, corresponding to the (211) plane of Li_2Ga_7 (PDF# 04-007-0673, R-3m). Subsequently, the Li_2Ga_7 peak vanishes, and peaks at 3.87˚, 6.3˚, and 7.4˚ appear, associated with the (111), (220), and (311) planes of LiGa (PDF# 03-065-1072, Fd-3m), respectively. The orthorhombic Li_2Ga phase is not formed at the end of the discharge process. Due to the relatively high C-rate employed in this in-situ XRD experiment, the final lithiation stage below 0.25V, converting LiGa to Li_2Ga, is not observed. Previous studies have reported that the formation of Li_2Ga from LiGa is not likely to

take place without enough kinetic conditions such as very low current and high temperature [31, 32]. As shown in Fig. 2a, these LiGa peaks shift to lower angles and increase in intensity, indicating slight lattice expansion as Li ions intercalate into the LiGa crystal, which is a process of solid solution formation [31]. Throughout this lithiation phase, only gallium shows Li storage activity, with indium remaining inactive. Upon charging, the LiGa peaks revert to higher angles and begin to diminish. At 0.65 V, the Li_2Ga_7 peak reappears, then gradually fades with continued charging. Due to the relatively high C rate, the Li_2Ga_7 peak did not disappear at the end of charge, demonstrating the incomplete conversion from Li_2Ga_7 to GaIn.

Integrating findings from both the literature and our experiments, without the lithiation step from LiGa to Li_2Ga, which is happening at a very lower potential vs Li/Li^+(~0V), it can only demonstrate half of its theoretical capacity. In the solid-state cell constructed in this work, solid electrolytes function both as pathways for Li ions and as separators between the cathode and anode in batteries. The sulfide-based solid electrolyte used in this study, Li_6PS_5Cl, exhibit notable characteristics, including high ionic conductivity and low mechanical stiffness. However, this sulfide electrolyte encounters compatibility issues with Li metal, leading to instability. To overcome this challenge, two main approaches have been adopted: one involves applying a protective buffer layer to shield the Li, and the other entails replacing Li with an alternative Li resource material that is compatible with sulfide electrolytes. In this study, Li metal is substituted with a Li-Al alloy to enhance compatibility and mitigate electrolyte instability. Given our use of Li-Al alloy as the reference electrode in our SSB-H system, rather than Li metal, we observe that our SSB-H can deliver only about half of the theoretical capacity. This reduction is due to the potential difference of approximately 0.34 V between the Li-Al alloy and Li metal [33, 34]. This finding aligns with our experimental observations, where the potential difference between Li-Al and Li metal remained around 0.36V during extended discharging cycles (Fig. S3). Therefore, the Li-Al alloy can be considered a stable reference electrode, maintaining a potential gap of 0.36V with respect to Li throughout the charging and discharging cycles of our SSB-H. Consequently, the theoretical capacity of our Ga-In SSB-H system is estimated to be around 384.5 mAh g^{-1}. Li-In can also be used to substitute Li metal for Li_6PS_5Cl-based SSBs. We chose Li-Al over Li-In because Li-Al has a lower voltage plateau (0.36 V vs. Li+/Li) compared to Li-In (0.6 V vs. Li+/Li).[35] The lower voltage of Li-Al allows the Ga-In alloy to achieve a higher capacity.

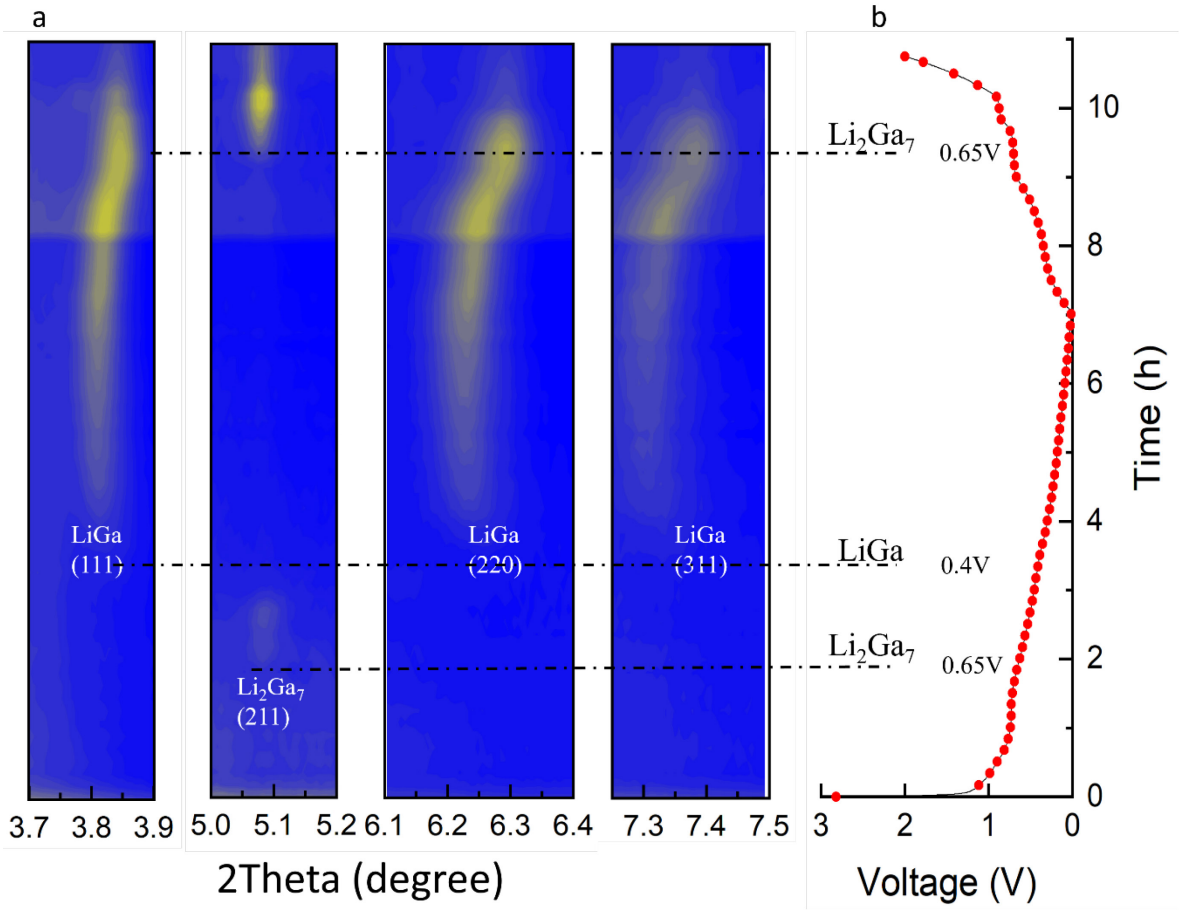
a
b
LiGa
(111)
LiGa
(220)
LiGa
(311)
Li2Ga7
(211)
Li2Ga7
0.65V
LiGa
0.4V
Li2Ga7
0.65V
3.7 3.8 3.9 5.0 5.1 5.2 6.1 6.2 6.3 6.4 7.3 7.4 7.5
2Theta (degree)
3 2 1 0
Voltage (V)
0 2 4 6 8 10
Time (h)

Figure 2. a) In-situ XRD pattern contour map of the Ga-In electrode in a liquid in-situ coin cell; b) Voltage profile of the liquid in-situ coin cell during the in situ XRD experiment.

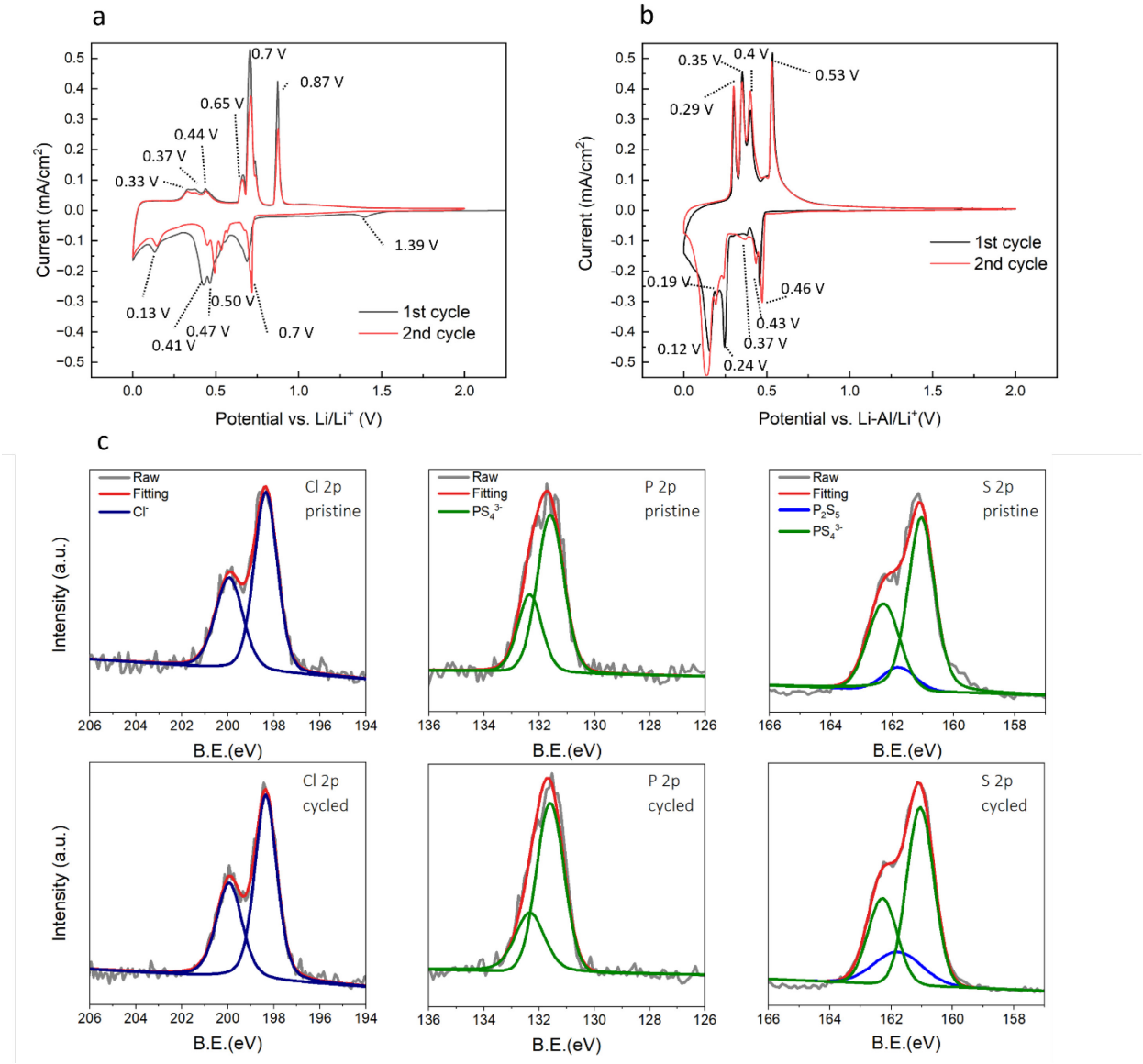

Figure 3. a) CV graph for a Ga-In electrode with Li metal in a liquid electrolyte coin cell; b) CV graph for a Ga-In electrode with Li-Al in an SSB-H; c) XPS analysis of electrolyte pristine Li_6PS_5Cl and cycled Li_6PS_5Cl.

The electrochemical behavior of the Ga-In alloy was assessed using CV in half-cells using Li metal as the reference electrode, operating at a scan rate of 0.1 mV s^{-1}, as depicted in Fig. 3a. In the initial cathodic sweep from the open-circuit voltage (OCV) to 0.01 V, a broad and irreversible peak at

1.39 V was observed, indicating SEI formation. Subsequent Li insertion peaks at 0.7 V, and 0.50 V, 0.47 V, 0.41 V, and 0.13 V correspond to the formation of Li_2Ga_7, and LiGa, and Li_2Ga, respectively. During the anodic sweep, peaks at 0.34 V, 0.37 V and 0.44 V were related to Li extraction from Li_2Ga to LiGa, while peaks at 0.65 V and 0.7 V were linked to the extraction from LiGa to Li_2Ga_7. The peak at 0.87 V was associated with Li extraction from Li_2Ga_7 back to Ga-In liquid metal. Contrasting with a liquid coin cell, the CV of the SSB-H in a Li-Al half cell (Fig. 3b) exhibited peaks at a lower voltage range, reflecting the voltage difference between Li metal and the Li-Al alloy. Notably, no irreversible SEI formation peak appeared during the initial cathodic sweep. In this sweep, peaks at 0.46 V, 0.43 V, and 0.37 V were linked to Li insertion forming Li_2Ga_7, while peaks at 0.14 V, 0.19 V, and 0.24 V were related to LiGa formation. Anodic peaks at 0.29 V, 0.35 V, and 0.40 V corresponded to the Li extraction from LiGa to Li_2Ga_7, and the peak at 0.53 V related to the extraction from Li_2Ga_7 back to Ga-In liquid metal. The CV peaks of SSB-H exhibit stable behavior, showing shifts of 0.01-0.02V between the first and the second cycles. These slight shifts may be attributed to the structure change in Li-Al and the alternations in state of Ga-In alloy from liquid to solid. No significant peaks associated with indium de/lithiation were observed in the CV scans, either with or without a solid electrolyte, aligning with the findings from operando XRD experiments. To further assess the electrochemical stability of the Li_6PS_5Cl electrolyte, XPS analysis was performed on both pristine and cycled samples (see Fig. 3c). No significant differences were detected between the pristine and cycled Li_6PS_5Cl. However, in the S 2p spectrum, the cycled Li_6PS_5Cl showed a slight increase in P_2S_5, a product of the oxidative decomposition of Li_6PS_5Cl during the charging process to transfer Li-ions[36, 37]. Overall, the Li-Ga

alloying reaction accounts for the full capacity, with no significant side reactions detected at the electrode/electrolyte interface.

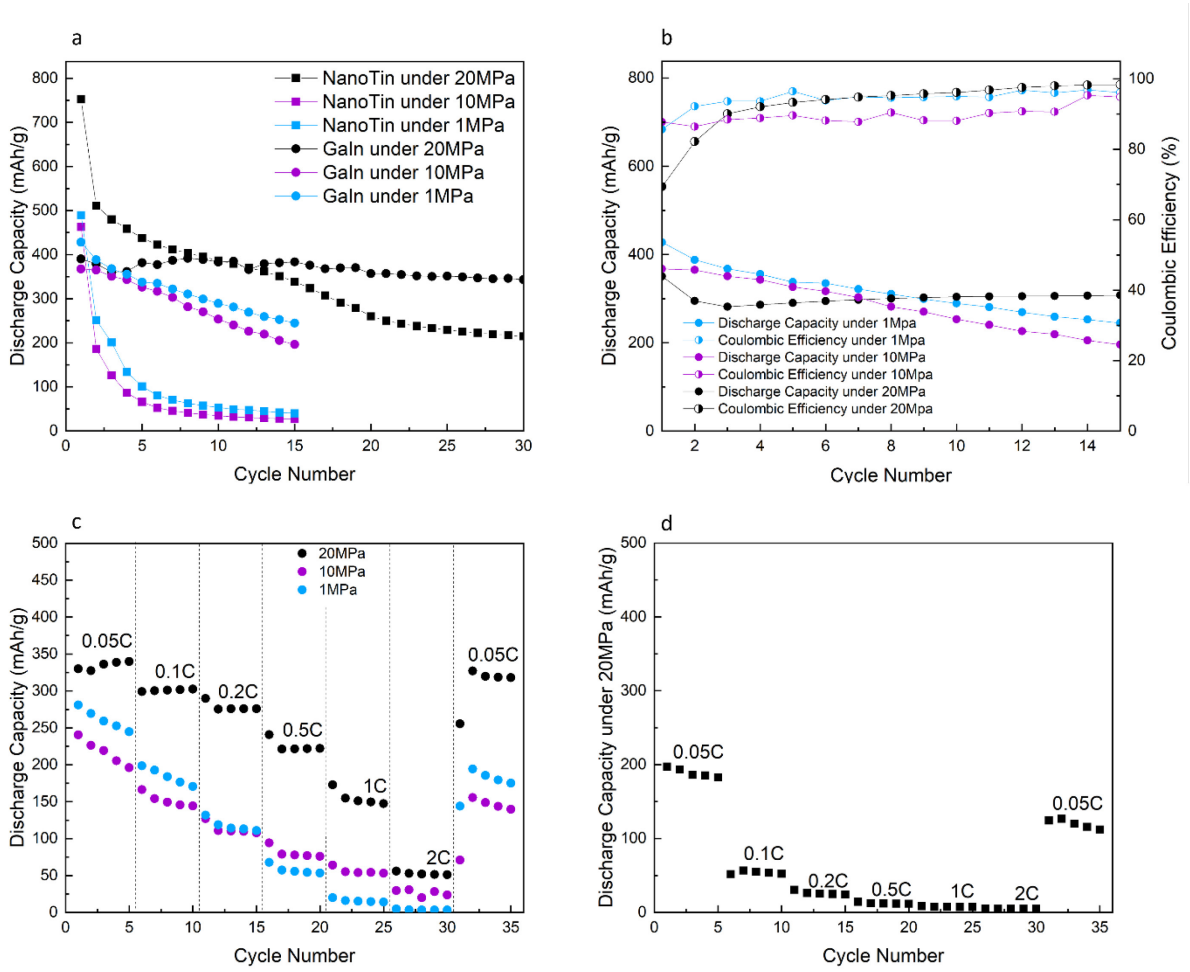

Figure 4. a) Comparison of the cycling performance between Ga-In alloy and nano-Sn in SSB-H at varying pressures. Coulombic efficiency data are shown in Fig. S5a; b) Coulombic efficiency of Ga-In SSB-Hs under different pressures. Charge/Discharge profiles of initial cycles are shown in Fig. S6; c) Rate capability of Ga-In SSB-Hs under different pressures. Coulombic efficiency data are shown in Fig. S5b; d) Rate capability of a nano-Sn SSB-H under 20 MPa pressures.

Fig. 4a depicts the cycling performance of the Ga-In SSB-H at a rate of 0.05 C under varying stack pressures, in comparison with nano-sized Sn. Both materials exhibited optimal performance at 20 MPa. The Ga-In alloy maintained a relatively stable capacity, reaching approximately 343 mAh g^{-1} at the 30th cycle, which is 88% of its initial capacity of 389 mAh g^{-1}. In contrast, nano-sized Sn

delivered only 214 mAh g^{-1} at the 30th cycle, or 28.5% of its initial capacity of 752 mAh g^{-1}. The Ga-In liquid metal demonstrated superior performance under lower pressures, retaining 53% of its initial capacity at the 15th cycle under 10 MPa, and 57% under 1 MPa, while Sn maintained just 7% and 5%, respectively. The reduced capacity loss of Ga-In could result from diminished interfacial contact disruption caused by volume changes during cycling. This preservation of interfacial contact, especially under 20 MPa, leads to improved cycling stability. Cycling performance and coulombic efficiency of the Ga-In alloy under varying pressures are further illustrated in Fig. 4b. At lower pressures, coulombic efficiency exhibited fluctuations due to unstable contact. However, at 20 MPa, the efficiency increased steadily, approaching 100%. Initial cycling at high pressure led to lower initial efficiency, potentially due to the gradual disconnection of weakly adhered Ga-In particles. Applying high pressure during the first cycle caused the expulsion of Ga-In particles that were weakly connected to the current collector, while stabilizing the remaining connections. This led to a decrease in capacity during the initial cycles, followed by a slight increase and subsequent stabilization.

Fig. 4c highlights the rate capability of Ga-In SSB-Hs, which were tested at 0.05 C for 15 cycles and achieved a capacity around 340 mAh g^{-1} under 20 MPa pressure, 240mAh g^{-1} under 10 MPa pressure, and 280 mAh g^{-1} under 1 MPa pressure, respectively. As the rate increased from 0.05 C to 2 C under 20 MPa, the discharge capacity decreased from 329 mAh g^{-1} to 51 mAh g^{-1}, but recovered to 327 mAh g^{-1} when the rate returned to 0.05 C. In contrast, under low pressures, the discharge capacities showed significant reductions when the rate was decreased back to 0.05 C, reflecting the trends in cycling performance. Notably, at higher rates (0.5 C, 1 C and 2 C), the discharge capacity under 10 MPa exceeded that under 1 MPa, although initially the electrode under 1 MPa showed higher capacity. This underscores the crucial role of stack pressure in maintaining cycling stability, especially at higher currents. Fig. 4d shows the rate capability of a cycled nano-Sn electrode under 20 MPa. Initially it was cycled for 30 cycles at 0.05 C. During the rate capacity test, the cell experienced a decrease in discharge capacity from nearly 200 mAh g^{-1} to about 5 mAh g^{-1} as the C-rate increased to 2 C. When the C-rate returned to 0.05 C, the discharge capacity was around 125 mAh g^{-1}, consistent with its overall cycling performance. The rate capability results clearly demonstrate that Ga-In liquid metal electrode maintains better interfacial contact than solid

active materials in SSB setups, which facilitates Li ion transport between the active materials and solid electrolytes.

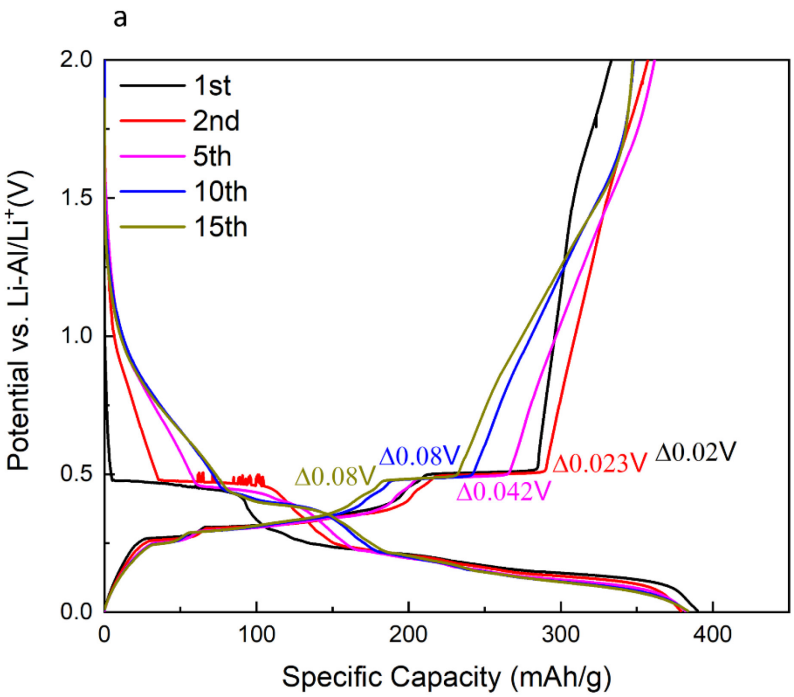

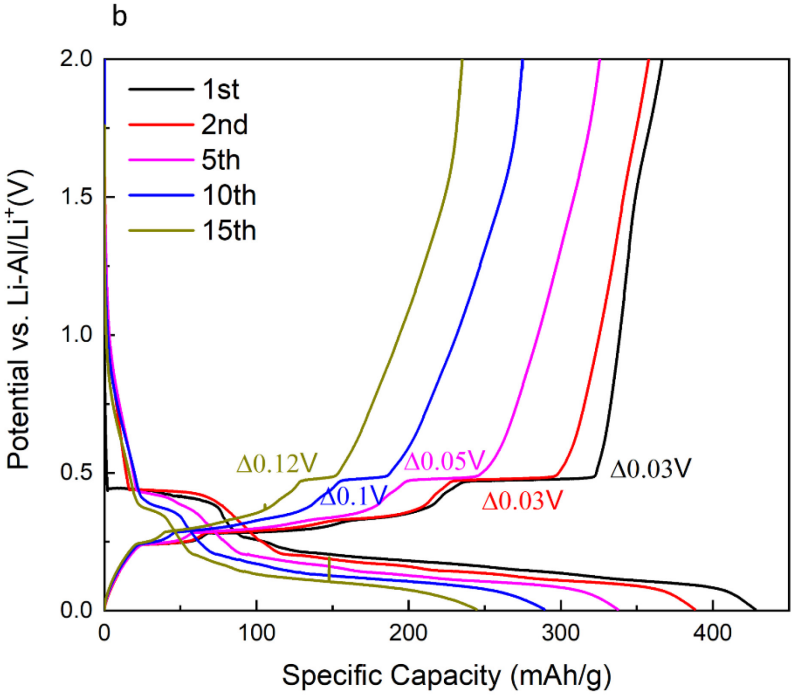

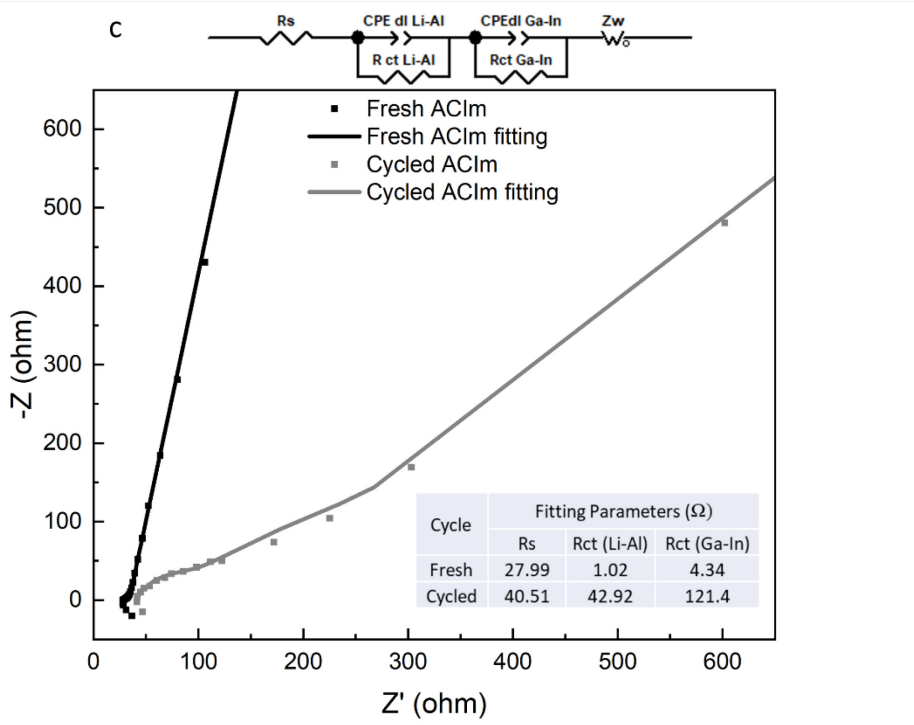

Figure 5. a) Voltage profiles of a Ga-In SSB-H at 20MPa pressure; b) Voltage profiles of a Ga-In SSB-H at 1MPa pressure; c) EIS analysis of a Ga-In SSB-H. It includes the equivalent circuit model for EIS fitting, Nyquist plots, and resistance fitting outcomes.

Figures 5a and b illustrate the voltage profiles of a Ga-In SSB-H under pressures of 20 MPa and 1 MPa, respectively. In Fig. 5a, the voltage plateaus correlate well with the peaks observed in the CV results shown in Fig. 3b. This correlation is further supported by the dQ/dV curves shown in supplementary Fig. S4. The peaks in this figure align with those in Fig. 3b, reinforcing the consistent performance of the Ga-In liquid metal electrode. Figures 5a and b also highlight noticeable voltage discrepancies, particularly around 0.4 V, between the charging and discharging plateaus. The Ga-In alloy demonstrates stable performance, which is more pronounced under higher pressures. Under low pressure (1 MPa), the hysteresis expanded from 0.03 V to 0.12 V from cycle 1 to 15, possibly due to deteriorating contact during cycling. The observed hysteresis expansion under lower pressure suggests that mechanical stability is crucial for maintaining efficient ion transport and electrical contact within the SSB. Fig. S5 c and d show a more pronounced hysteresis expansion of voltage plateaus of Sn SSB-H under pressures of 20 MPa and 1 MPa. The pressure-dependent performance implies that the Ga-In alloy, with its inherent self-

healing and fluid characteristics, can adapt better to the internal stresses and maintain a more stable interfacial contact, especially under optimized pressure conditions.

To study the changes in the resistance of the liquid alloy contact area, AC impedance measurements were conducted on Ga-In SSB-Hs at various stages of cycling. The raw Electrochemical Impedance Spectroscopy (EIS) data presented in Fig. S7 exhibit noise in the mid-frequency region, which we attribute to the transition from liquid to solid during the lithiation process. This phase change likely causes considerable alterations at the interface between the Ga-In droplets and the solid electrolyte. Fig. 5c represents an improved version of Fig. S7 a and b, where the data points of outlier have been eliminated. As shown in Fig. 5c, there is a noticeable increase in the resistance of the Ga-In SSB-H from the initial to the 30th cycle. These impedance measurements were taken in a battery configuration using a Li-Al alloy instead of Li metal, meaning that both electrodes significantly contribute to the overall impedance. Literature suggests that the relative contribution of each electrode to the impedance depends on the state of charge [38-40]. In our experiments, the impedance spectra were recorded at the fully delithiated state, where Li ions are predominantly at the Li-Al electrode, making its impedance contribution larger than that of the Ga-In electrode. Specifically, the electrolyte resistance (Rs) escalated from 27.99 Ω at the first cycle to 40.51 Ω at the 30th cycle. Additionally, the charge transfer resistance (Rct) at the Ga-In electrode increased from 1.02 Ω at the first cycle to 42.92 Ω at the 30th cycle. There is also an increase in the AC impedance component, the charge transfer resistance due to the Li-Al electrode, which rose from 4.34 Ω to 121.4 Ω. This suggests that the contact area within the battery decreases over the cycling process, likely as a result of the volume changes occurring in the Ga-In droplets. The Ga-In liquid electrode requires optimization to address the issue of increasing interfacial resistance. For comparison, Fig. S7c shows that the impedance of Sn SSB-H increased after cycling. Because it does not have the transition between liquid state and solid state, Fig. S7c does not exhibit noise in the mid-frequency region. While the impedance of the Ga-In SSB-H increases during cycling, it remains much higher capacity compared to solid electrode SSB-Hs, such as those with Sn electrodes. It suggests that the inherent fluidity and adaptable interfacial contact of the liquid metal alloy used in the Ga-In electrode help to keep a better ionic conductivity and less resistance to charge transfer relatively.

The cycling and rate capacity data indicate that the Ga-In liquid metal alloy is more suitable for SSB operation at lower pressures compared to Sn. At 1 MPa, the Ga-In electrode maintains a significant capacity, albeit with some reduction, while the capacity of Sn diminishes almost completely to nearly 0 mAh g^{-1}. At a high pressure of 20 MPa and a cycling rate of 0.5 C, the Ga-In SSB-H retains about 60% of its initial capacity observed at 0.05 C, while the capacity of the Sn SSB-H is nearly depleted. These results highlight the superior adaptability and performance of liquid metal alloys like Ga-In in SSBs under varied pressure conditions, highlighting their potential as robust anode materials for future SSB development.

The long-term cycling performance of the Ga-In SSB-H under 20 MPa was investigated, as shown in Fig. 6. This figure highlights the Ga-In liquid metal electrode's significant stability through numerous cycles and under elevated cycling rates. Initially, the cell underwent 25 cycles at a 0.05 C rate, followed by an extended cycling phase of 500 cycles at a 0.5 C rate. Despite the expected capacity reduction associated with increased cycling rates, the battery cell exhibited remarkable cycling stability, retaining approximately 66% of its original capacity. The capacity decreased from 300 mAh g^{-1} at the beginning to 198 mAh g^{-1} at the 500th cycle at a 0.5 C rate. In addition, the Coulombic efficiency maintained almost 100% for the 0.5 C cycling.

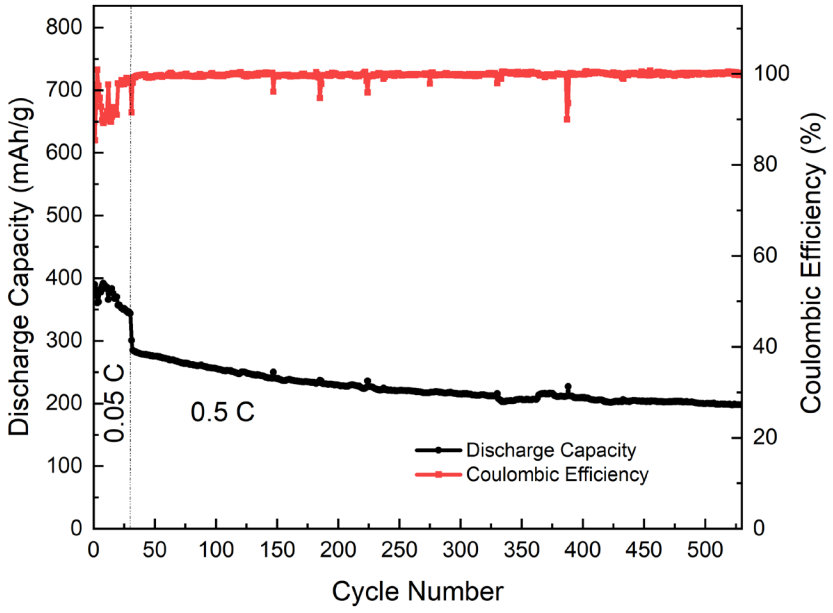

Figure 6. Long-term cycling performance of a Ga-In SSB-H under 20 MPa at 0.5 C, initially activated at a rate of 0.05 C and subsequently cycled at 0.5 C.

To explore how stack pressure and structural changes interact during the cycling of Ga-In liquid metal versus solid Sn, we monitored the stack pressure changes during the lithiation and delithiation processes of nano-Sn and Ga-In electrodes. Fig. 7 displays the corresponding variations in voltage and pressure, with Fig. 7a illustrating the pattern for a nano-Sn SSB-F using NMC111 as the cathode, and Fig. 7b showing the pattern for a Ga-In SSB-F. The choice of NMC111 over a Li-Al alloy was made to mitigate the significant volume changes experienced by the latter during cycling. Both Sn and Ga-In exhibited three distinct voltage plateaus, corresponding to the sequential formation of Li_2Sn_5, LiSn, Li_xSn ($1<x\leqslant 4.4$) for Sn, and Li_2Ga_7, LiGa, Li_2Ga for Ga-In, respectively. As shown in Fig. 7c, during the initial stage of lithiation, the pressure within the Sn SSB-F decreases during the formation of Li_2Sn_5, which has been consistently observed across a series of pressure monitoring tests conducted during Sn SSB-F lithiation. This phenomenon appears to contradict the expected increase in stack pressure due to volume expansion during the transition from Sn to Li_2Sn_5. However, it has been reported in literature that lithiation reduces the elastic modules and fracture resistance of Li-Sn alloys [41, 42].

The initial stack pressure applied to these Sn SSB-F cells exceeds the yield strength of both Sn and Li-Sn alloys. Fig. 8a displays Sn nanoparticles in a pristine Sn electrode, highlighting that under high pressing pressure, the Sn nanoparticles did not form a solid mass and retained voids and their spherical shape. Since lithiation softens Sn particles, it is likely that lithiated Sn deforms plastically to fill these voids, leading to a decrease in stack pressure. Fig. 8b, an SEM image of a Sn electrode after the first cycle, shows the transformation of spherical Sn particles into irregular shapes and the near disappearance of voids among particles. As shown in Fig. 7a, after the voids were filled by the deformed Li-Sn alloy, the stack pressure started to increase due to the volume increase caused by lithiation. After the initial pressure drop, the pressure profile of Sn during lithiation exhibited two distinct rates of increase. Initially, up to the LiSn formation plateau, the pressure rise was relatively slow. However, during the final lithiation phase to form Li_xSn ($1<x\leqslant 4.4$), the rate of pressure increase accelerated significantly. It surged from 0.46 MPa at 56% normalized capacity to 3.07 MPa at 100% normalized capacity, indicating a significant structural transformation during this phase.

For the Ga-In SSB-F, the pressure trend closely aligned with the voltage profile. As shown in Fig. 7d, it began with a sharp increase as the liquid Ga-In transitioned to solid, followed by a leveling off to slower growth as Li_2Ga_7 formed from the liquid metal. After LiGa formation, the pressure rise accelerated again during the solid solution formation process, as more Li was inserted into LiGa. This increase moved from 0.61 MPa at 58% normalized capacity to 1.07 MPa at 82% normalized capacity. During the formation of Li_2Ga, a modest increase in pressure was observed, from 1.07 MPa at 82% normalized capacity to 1.23 MPa at 100% normalized capacity. The varying rates of pressure change from LiGa to Li_2Ga are likely due to the transformation from 3D (LiGa) to 2D (Li_2Ga) [43]. The rate of volume change 3D LiGa during the solid solution formation is higher than that of the LiGa to Li_2Ga transformation. When comparing the most rapid pressure increasing rates between Sn and Ga-In SSB-Fs, Sn's rate (5.93 MPa change per normalized capacity) exceeded Ga-In's (1.91 MPa change per normalized capacity). Moreover, the total pressure increase for Ga-In (1.23 MPa) was less than that for Sn (3.7 MPa), despite Sn experiencing an approximate 260% volume change and Ga-In a 120% (Pure Ga has about 160% volume change) volume change throughout the process [44-46]. This indicates that the fluid nature of liquid metal better utilizes porosity to mitigate the effects of volume expansion.

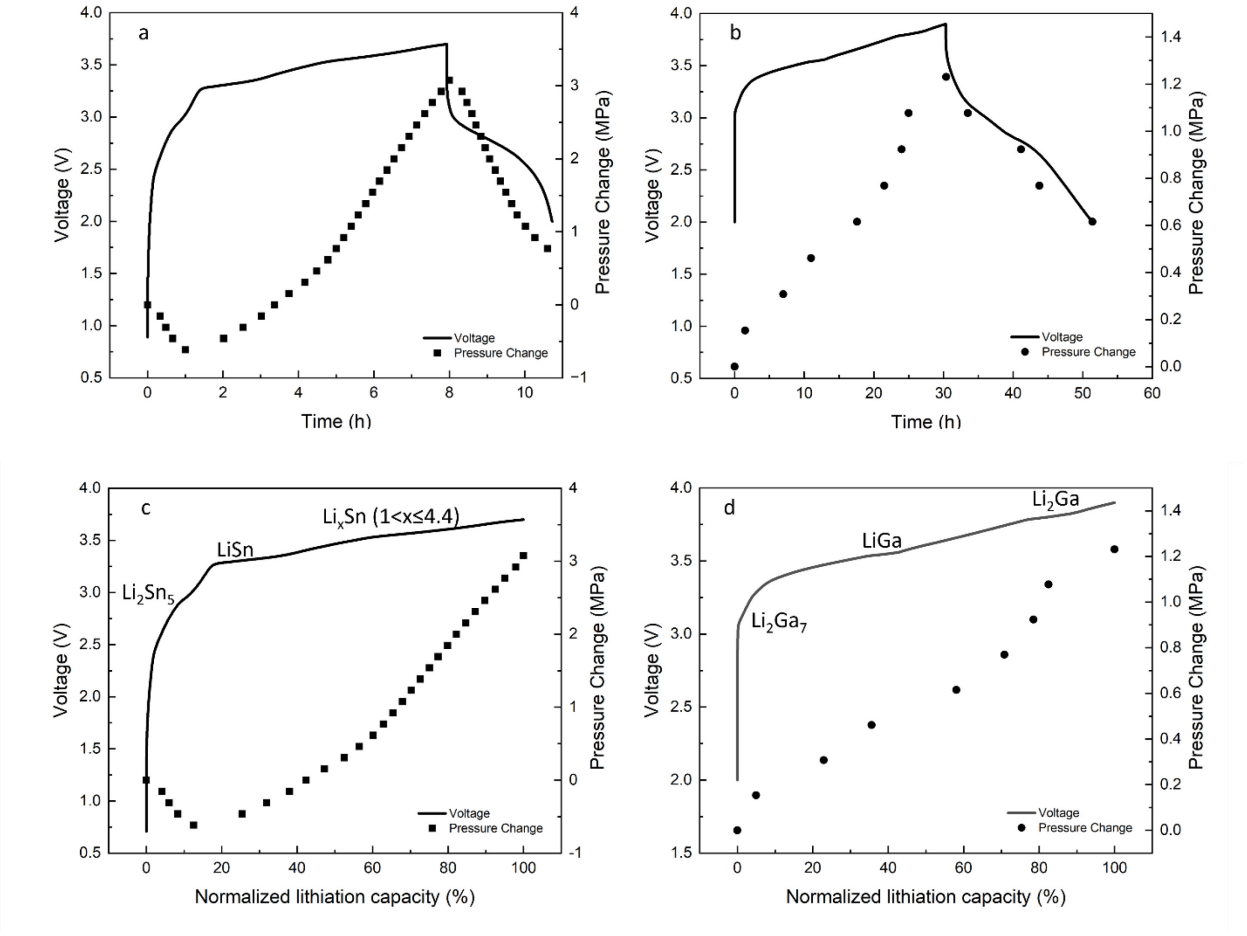

Figure 7. Pressure and voltage variation patterns for nano-Sn and Ga-In SSB-Fs during cycling and lithiation processes. (a) Nano-Sn SSB-F during a full cycle; (b) Ga-In SSB-F during a full cycle; (c) Nano-Sn SSB-F during lithiation; (d) Ga-In SSB-F during lithiation.

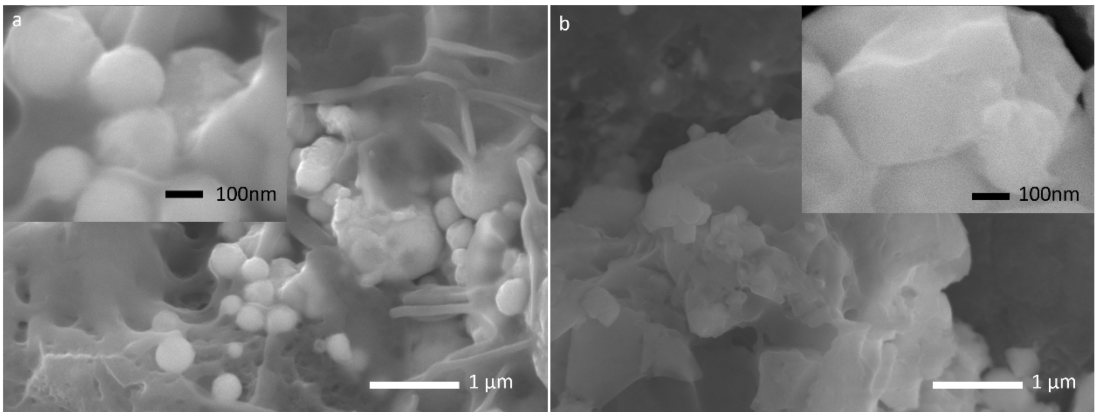

Figure 8. SEM images of pressed Sn electrodes, a) pristine Sn electrode; b) cycled Sn electrode.

Conclusion

In this study, we demonstrated that employing a Ga-In liquid metal alloy as the active material significantly boosts the cycling stability of SSBs. Through comparative analyses of the cycling stability and rate capacity of the Ga-In liquid alloy anode against solid active materials, we confirmed that the self-healing properties and fluid nature of the alloy ensure sustained interfacial contact with solid electrolytes. This interaction is crucial for enhancing the cycling stability and rate capacity, particularly at reduced stack pressures. In-situ XRD investigations revealed that indium does not participate in the lithiation/delithiation process; instead, it aids in maintaining the alloy's low melting point, facilitating its return to a liquid state after delithiation. Through monitoring stack pressure, we determined that stress levels fluctuate with structural changes. The Ga-In liquid metal exhibited the ability to buffer pressure increases caused by deformation during lithiation, highlighting its adaptability under mechanical stress. Despite the promising properties of Ga-In alloys for SSB applications, their high cost poses significant barriers to large-scale commercialization. Overcoming these challenges will require reducing reliance on these materials or developing alternative materials that provide similar benefits at lower economic costs. However, this research provides valuable insights into the potential of liquid metal alloys in improving the performance of SSBs.

Supporting Information

In-situ XRD plots of the Ga-In electrode in a liquid in-situ coin cell, voltage profile of Li-Al vs Li metal during constant current delithiation, dQ/dV plots of Ga-In alloy in an SSB-H under 20 MPa, Coulombic efficiency of SSB-Hs, Galvanostatic charge/discharge profiles of initial cycle of Ga-In SSB-Hs under different pressures, Nyquist plot of SSB-Hs, and measurement of the contact angle of the Ga-In liquid alloy on the solid electrolyte surface.

Acknowledgments

This material is based upon work supported by the National Science Foundation under Grants No. 2323474 and No. 2323475. Any opinions, findings, and conclusions or recommendations expressed in this material are those of the author(s) and do not necessarily reflect the views of the National Science Foundation. This research used resources of the Advanced Photon Source, a U.S. Department of Energy (DOE) Office of Science user facility operated for the DOE Office of Science by Argonne National Laboratory under Contract No. DE-AC02-06CH11357. X.C.C. is sponsored by the U.S. Department of Energy (DOE), Office of Energy Efficiency and Renewable Energy for the Vehicle Technologies Offices Advanced Battery Materials Research Program.

Reference

(1) Armand, M.; Tarascon, J. M. Building Better Batteries. *Nature* **2008**, *451* (7179), 652-657.
(2) Wu, J.; Shen, L.; Zhang, Z.; Liu, G.; Wang, Z.; Zhou, D.; Wan, H.; Xu, X.; Yao, X. All-Solid-State Lithium Batteries with Sulfide Electrolytes and Oxide Cathodes. *Electrochem. Energy Rev.* **2021**, *4*, 101-135.
(3) Chen, S.; Xie, D.; Liu, G.; Mwizerwa, J. P.; Zhang, Q.; Zhao, Y.; Xu, X.; Yao, X. Sulfide Solid Electrolytes for All-Solid-StateLithium Batteries: Structure, Conductivity, Stability and Application. *Energy Storage Mater.* **2018**, *14*, 58-74.
(4) Wu, J.; Liu, S.; Han, F.; Yao, X.; Wang, C. Lithium/Sulfide All‐Solid‐State Batteries Using Sulfide Electrolytes. *Adv. Mater.* **2021**, *33* (6), 2000751.
(5) Klavetter, K. C.; de Souza, J. P.; Heller, A.; Mullins, C. B. High Tap Density Microparticles of Selenium-Doped Germanium as a High Efficiency, Stable Cycling Lithium-Ion Battery Anode. *J. Mater. Chem. A* **2015**, *3* (11), 5829-5834.
(6) Müller, S.; Pietsch, P.; Brandt, B.; Baade, P.; De Andrade, V.; De Carlo, F.; Wood, V. Quantification and Modeling of Mechanical Degradation in Lithium-Ion Batteries Based on Nanoscale Imaging. *Nat. Commun.* **2018**, *9*, 2340.
(7) Zhou, X. W.; Li, T. Y.; Cui, Y.; Fu, Y. Z.; Liu, Y. Z.; Zhu, L. In Situ Focused Ion Beam Scanning Electron Microscope Study of Microstructural Evolution of Single Tin Particle Anode for Li-Ion Batteries. *ACS Appl. Mater. Interfaces* **2019**, *11* (2), 1733-1738.
(8) Lim, L. Y.; Liu, N.; Cui, Y.; Toney, M. F. Understanding Phase Transformation in Crystalline Ge Anodes for Li-Ion Batteries. *Chem. Mater.* **2014**, *26* (12), 3739-3746.
(9) Lim, L. Y.; Fan, S. F.; Hng, H. H.; Toney, M. F. Storage Capacity and Cycling Stability in Ge Anodes: Relationship of Anode Structure and Cycling Rate. *Adv. Energy Mater.* **2015**, *5* (15), 1500599.
(10) Li, T. Y.; Zhou, X. W.; Cui, Y.; Lim, C.; Kang, H. X.; Yan, B.; Wang, J. J.; Wang, J.; Fu, Y. Z.; Zhu, L. K. Characterization of Dynamic Morphological Changes of Tin Anode Electrode during (De)lithiation Processes Using in Operando Synchrotron Transmission X-ray Microscopy. *Electrochim. Acta* **2019**, *314*, 212-218.

(11) Wang, J. J.; Chen-Wiegart, Y. C. K.; Wang, J. In Situ Three-Dimensional Synchrotron X-Ray Nanotomography of the (De) lithiation Processes in Tin Anodes. *Angew Chem. Int. Edit.* **2014**, *53* (17), 4460-4464.
(12) Wang, J. J.; Chen-Wiegart, Y. C. K.; Eng, C.; Shen, Q.; Wang, J. Visualization of Anisotropic-Isotropic Phase Transformation Dynamics in Battery Electrode Particles. *Nat. Commun.* **2016**, *7*, 12372.
(13) Zhang, W. J. A Review of the Electrochemical Performance of Alloy Anodes for Lithium-Ion Batteries. *J. Power Sources* **2011**, *196* (1), 13-24.
(14) Li, C.; Wang, Z. Y.; He, Z. J.; Li, Y. J.; Mao, J.; Dai, K. H.; Yan, C.; Zheng, J. C. An Advance Review of Solid-State Battery: Challenges, Progress and Prospects. *Sustain. Mater. Techno.* **2021**, *29*, e00297
(15) Wu, Y. P.; Huang, L.; Huang, X. K.; Guo, X. R.; Liu, D.; Zheng, D.; Zhang, X. L.; Ren, R.; Qu, D. Y.; Chen, J. H. A Room-Temperature Liquid Metal-Based Eelf-Healing Anode for Lithium-Ion Batteries with an Ultra-Long Cycle Life. *Energ. Environ. Sci.* **2017**, *10* (8), 1854-1861.
(16) Yao, X. Y.; Huang, N.; Han, F. D.; Zhang, Q.; Wan, H. L.; Mwizerwa, J. P.; Wang, C. S.; Xu, X. X. High-Performance All-Solid-State Lithium-Sulfur Batteries Enabled by Amorphous Sulfur-Coated Reduced Graphene Oxide Cathodes. *Adv. Energy Mater.* **2017**, *7* (17), 1602923.
(17) Lee, Y. G.; Fujiki, S.; Jung, C. H.; Suzuki, N.; Yashiro, N.; Omoda, R.; Ko, D. S.; Shiratsuchi, T.; Sugimoto, T.; Ryu, S.; Ku, J. H.; Watanabe, T.; Park, Y.; Aihara, Y.; Im, D.; Han, I. T. High-Energy Long-Cycling All-Solid-State Lithium Metal Batteries Enabled by Silver-Carbon Composite Anodes. *Nat. Energy* **2020**, *5* (4), 348-348.
(18) Koerver, R.; Zhang, W. B.; de Biasi, L.; Schweidler, S.; Kondrakov, A. O.; Kolling, S.; Brezesinski, T.; Hartmann, P.; Zeier, W. G.; Janek, J. Chemo-Mechanical Expansion of Lithium Electrode Materials - on the Route to Mechanically Optimized All-Solid-State Batteries. *Energ. Environ. Sci.* **2018**, *11* (8), 2142-2158.
(19) Jun, S.; Nam, Y. J.; Kwak, H.; Kim, K. T.; Oh, D. Y.; Jung, Y. S. Operando Differential Electrochemical Pressiometry for Probing Electrochemo-Mechanics in All-Solid-State Batteries. *Adv. Funct. Mater.* **2020**, *30* (31), 2002535.
(20) Doux, J. M.; Nguyen, H.; Tan, D. H. S.; Banerjee, A.; Wang, X. F.; Wu, E. A.; Jo, C.; Yang, H. D.; Meng, Y. S. Stack Pressure Considerations for Room-Temperature All-Solid-State Lithium Metal Batteries. *Adv. Energy Mater.* **2020**, *10* (1), 1903253.
(21) Obrovac, M. N.; Christensen, L.; Le, D. B.; Dahnb, J. R. Alloy Design for Lithium-Ion Battery Anodes. *J. Electrochem. Soc.* **2007**, *154* (9), A849-A855.
(22) Banerjee, A.; Wang, X. F.; Fang, C. C.; Wu, E. A.; Meng, Y. S. Interfaces and Interphases in All-Solid-State Batteries with Inorganic Solid Electrolytes. *Chem. Rev.* **2020**, *120* (14), 6878-6933.
(23) Doux, J. M.; Yang, Y. Y. C.; Tan, D. H. S.; Nguyen, H.; Wu, E. A.; Wang, X. F.; Banerjee, A.; Meng, Y. S. Pressure Effects on Sulfide Electrolytes for All Solid-State Batteries. *J. Mater. Chem. A* **2020**, *8* (10), 5049-5055.
(24) Gao, X. W.; Liu, B. Y.; Hu, B. K.; Ning, Z. Y.; Jolly, D. S.; Zhang, S. M.; Perera, J.; Bu, J. F.; Liu, J. L.; Doerrer, C.; Darnbrough, E.; Armstrong, D.; Grant, P. S.; Bruce, P. G. Solid-State Lithium Battery Cathodes Operating at Low Pressures. *Joule* **2022**, *6* (3), 636-646.
(25) Mo, F. J.; Ruan, J. F.; Fu, W. B.; Fu, B. W.; Hu, J. M.; Lian, Z. X.; Li, S. Y.; Song, Y.; Zhou, Y. N.; Fang, F.; Sun, G.; Peng, S.; Sun, D. Revealing the Role of Liquid Metals at the

Anode-Electrolyte Interface for All Solid-State Lithium-Ion Batteries. *ACS Appl. Mater. Interfaces* **2020**, *12* (34), 38232-38240.
(26) Deshpande, R. D.; Li, J. C.; Cheng, Y. T.; Verbrugge, M. W. Liquid Metal Alloys as Self-Healing Negative Electrodes for Lithium Ion Batteries. *J. Electrochem. Soc.* **2011**, *158* (8), A845-A849.
(27) Liang, W. T.; Hong, L.; Yang, H.; Fan, F. F.; Liu, Y.; Li, H.; Li, J.; Huang, J. Y.; Chen, L. Q.; Zhu, T.; Zhang, S. Nanovoid Formation and Annihilation in Gallium Nanodroplets under Lithiation-Delithiation Cycling. *Nano. Lett.* **2013**, *13* (11), 5212-5217.
(28) Guo, X. L.; Zhang, L. Y.; Ding, Y.; Goodenough, J. B.; Yu, G. H. Room-Temperature Liquid Metal and Alloy Systems for Energy Storage Applications. *Energ. Environ. Sci.* **2019**, *12* (9), 2605-2619.
(29) Luo, T.; Wang, L.; Dai, L.; Luo, J.; Liu, S. A Solid-State Lithium Metal Battery with Extended Cycling and Rate Performance Using a Low-Melting Alloy Interface. *Inorg. Chem. Front.* **2023**, *10* (3), 1011-1017.
(30) Li, T. Y.; Cui, Y.; Fan, L. L.; Zhou, X. W.; Ren, Y.; De Andrade, V.; De Carlo, F.; Zhu, L. A Self-Healing Liquid Metal Anode with PEO-Based Polymer Electrolytes for Rechargeable Lithium Batteries. *Appl. Mater. Today* **2020**, *21*, 100802.
(31) Saint, J.; Morcrette, M.; Larcher, D.; Tarascon, J. M. Exploring the Li–Ga Room Temperature Phase Diagram and the Electrochemical Performances of the LixGay Alloys vs. Li. *Solid State Ionics* **2005**, *176* (1), 189-197.
(32) Lee, K. T.; Jung, Y. S.; Kwon, J. Y.; Kim, J. H.; Oh, S. M. Role of Electrochemically Driven Cu Nanograins in CuGa2 Electrode. *Chem. Mater.* **2008**, *20* (2), 447-453.
(33) Bang, H. J.; Kim, S.; Prakash, J. Electrochemical Investigations of Lithium-Aluminum Alloy Anode in Li/Polymer Cells. *J. Power Sources* **2001**, *92* (1-2), 45-49.
(34) Mohimont, F.; Le Ruyet, R.; Younesi, R.; Naylor, A. J. Study of the Electrochemical and Self-healing Processes of Galinstan as an Anode Material for Li-Ion Batteries. *J. Electrochem. Soc.* **2023**, *170* (5), 050535.
(35) Lu, P.; Xia, Y.; Sun, G.; Wu, D.; Wu, S.; Yan, W.; Zhu, X.; Lu, J.; Niu, Q.; Shi, S.; Sha, Z.; Chen, L.; Li, H.; Wu, F. Realizing Long-Cycling All-Solid-State Li-In||TiS2 Batteries Using Li6+xMxAs1-xS5I (M=Si, Sn) Sulfide Solid Electrolytes. *Nat. Commun.* **2023**, *14* (1), 4077.
(36) Kim, J.; Choi, W.; Hwang, S. J.; Kim, D. W. Incorporation of Ionic Conductive Polymers into Sulfide Electrolyte‐Based Solid‐State Batteries to Enhance Electrochemical Stability and Cycle Life. *Energy Environ. Mater.* **2024**, e12776.
(37) Tan, D. H.; Wu, E. A.; Nguyen, H.; Chen, Z.; Marple, M. A.; Doux, J.-M.; Wang, X.; Yang, H.; Banerjee, A.; Meng, Y. S. Elucidating Reversible Electrochemical Redox of Li6PS5Cl Solid Electrolyte. *ACS Energy Lett.* **2019**, *4* (10), 2418-2427.
(38) Abe, Y.; Hori, N.; Kumagai, S. Electrochemical Impedance Spectroscopy on the Performance Degradation of LiFePO4/Graphite Lithium-Ion Battery Due to Charge-Discharge Cycling under Different C-Rates. *Energies* **2019**, *12* (23), 4507.
(39) Wu, M. S.; Chiang, P. C. J.; Lin, J. C. Electrochemical Investigations on Advanced Lithium-Ion Batteries by Three-Electrode Measurements. *J. Electrochem. Soc.* **2005**, *152* (1), A47-A52.
(40) Hori, S.; Kanno, R.; Sun, X. Y.; Song, S. B.; Hirayama, M.; Hauck, B.; Dippon, M.; Dierickx, S.; Ivers-Tiffée, E. Understanding the Impedance Spectra of All-Solid-State Lithium Battery Cells with Sulfide Superionic Conductors. *J. Power Sources* **2023**, *556*, 232450.

(41) Zhang, P. P.; Ma, Z. S.; Jiang, W. J.; Wang, Y.; Pan, Y.; Lu, C. S. Mechanical Properties of Li-Sn Alloys for Li-Ion Battery Anodes: A First-Principles Perspective. *Aip. Adv.* **2016**, *6* (1), 015107.
(42) Zhang, P. P.; Ma, Z. S.; Wang, Y.; Zou, Y. L.; Lei, W. X.; Pan, Y.; Lu, C. S. A First Principles Study of the Mechanical Properties of Li-Sn Alloys. *RSC Adv.* **2015**, *5* (45), 36022-36029.
(43) Saint, J.; Morcrette, M.; Larcher, D.; Tarascon, J. M. Exploring the Li-Ga Room Temperature Phase Diagram and the Electrochemical Performances of the Li Ga Alloys vs. Li. *Solid State Ionics* **2005**, *176* (1-2), 189-197.
(44) Nam, H. G.; Park, J. Y.; Yuk, J. M.; Han, S. M. Phase Transformation Mechanism and Stress Evolution in Sn Anode. *Energy Storage Mater.* **2022**, *45*, 101-109.
(45) Winter, M.; Besenhard, J. O. Electrochemical Lithiation of Tin and Tin-based Intermetallics and Composites. *Electrochim. Acta* **1999**, *45* (1-2), 31-50.
(46) Zheng, X.; Guo, L.; Zhu, C. H.; Hu, T.; Gong, X. H.; Wu, C. G.; Wang, G. J.; Hou, Y. J. Preparation and Electrochemical Performance Study of a Self-Healing Electrode Composite Material with WSe2/Liquid Metal Galinstan for Lithium-Ion Batteries. *J. Alloy Compd.* **2023**, *969*, 172304.

Table of content